CrossMark

ORIGINAL PAPER

On the choice of parameters in the phase field method for simulating crack initiation with experimental validation

**T. T. Nguyen · J. Yvonnet · M. Bornert ·
C. Chateau · K. Sab · R. Romani · R. Le Roy**

Abstract The phase field method is a versatile simulation framework for studying initiation and propagation of complex crack networks without dependence to the finite element mesh. In this paper, we discuss the influence of parameters in the method and provide experimental validations of crack initiation and propagation in plaster specimens. More specifically, we show by theoretical and experimental analyses that the regularization length should be interpreted as a material parameter, and identified experimentally as it. Qualitative and quantitative comparisons between numerical predictions and experimental data are provided. We show that the phase field method can predict accurately crack initiation and propagation in plaster specimens in compression with respect to experiments, when the material parameters, including the characteristic length are identified by other simple experimental tests.

Keywords Crack initiation · Crack propagation · Simulation · Plaster · Digital image correlation

T. T. Nguyen · J. Yvonnet (✉)
Laboratoire Modélisation et Simulation Multi Échelle
MSME UMR 8208 CNRS, Université Paris-Est,
5 bd Descartes, 77454 Marne-la-Vallée, France
e-mail: julien.yvonnet@univ-paris-est.fr

T. T. Nguyen · M. Bornert · C. Chateau · K. Sab ·
R. Romani · R. Le Roy
Laboratoire Navier, CNRS UMR8205, ENPC, IFSTTAR,
Université Paris-Est, 6 et 8 avenue Blaise Pascal,
77455 Marne-la-Vallée, Cedex, France

1 Introduction

Simulation of crack initiation and growth in brittle materials such as concrete, cement or rocks is a major concern for predicting the strength and durability of structures made of these materials. One issue lies in the prediction of the onset of cracks in brittle materials: the classical Griffith theory of brittle fracture fails to predict crack initiation in un-notched specimens (Francfort and Marigo 1998). On the other hand, damage models with softening suffer from strong drawbacks when implemented in numerical solving methods such as the finite element method, like mesh dependency and lack of convergence of the fracture energy as the element size goes to zero (Pietruszczak and Mroz 1981; Bazant and Belytschko 1985). This has been shown to yield from a loss of ellipticity of the associated mechanical problem (Triantafyllidis and Aifantis 1986; Lasry and Belytschko 1988; De Borst et al. 1993). To circumvent these issues, regularization schemes must be applied, such as nonlocal damage models (Pijaudier-Cabot and Bazant 1987; Bazant and Pijaudier-Cabot 1988) and higher-order deformation gradient schemes (Peerlings et al. 1996; Lorentz and Benallal 2005). Another possibility is to introduce cohesive layers in the models which are then numerically solved via cohesive finite elements (Xu and Needleman 1994; Camacho and Ortiz 1996; Zhou and Molinari 2004). Cohesive elements require cracks to follow the element boundaries of the mesh. Other techniques like XFEM (Moës

et al. 1999; Belytschko and Black 1999; Daux et al. 2000) require a pre-existing crack and are not well adapted to complex cracks morphologies due to the underlying level-set functions needed to describe the displacement jump. Finally, we mention a new method, called Thick Level-Set method (TLS) (Bernard et al. 2012; Cazes and Moës 2015) in which a level-set function is employed to separate the undamaged zone from the damaged one, and where the crack is a consequence of the damage front motion, allowing crack initiation.

Recently, the phase field method has been proposed in Bourdin (2007), Eastgate et al. (2002), Francfort and Marigo (1998), Hakim and Karma (2009), Hofacker and Miehe (2013), Kuhn and Müller (2010), Miehe et al. (2010) and Spatschek et al. (2006) (only to name a few). It employs a diffuse approximation of discontinuities related to cracks and is consistent with brittle fracture through a modified variational principle. This technique is able to simulate brittle crack initiation and propagation without dependence to the mesh in a classical FEM framework. It allows handling very complex, multiple crack fronts and branching in both 2D and 3D without ad hoc numerical treatment. In Nguyen et al. (2015, 2016), the authors have demonstrated the capability of the method to simulate crack onset and propagation in complex image-based models, as such obtained by segmenting 3D X-Ray computed tomography images of real materials like concrete.

However, the method requires choosing a regularization parameter related to the smeared approximation of discontinuities. This parameter induces a characteristic length l in the model which must be chosen by the user. In Amor et al. (2009), he showed that a relationship can be established between l and at least two other material parameters. This seems consistent with a recent crack initiation criterion of Leguillon (2002) where two material parameters need to be identified for predicting crack onset. In the present work, we follow this line and show that l may be interpreted as a material parameter and should be deduced from experimental material parameters identification when available. We validate this by comparing simulations of crack initiation with experiments on drilled plaster samples, where the material parameters, including l, have been identified in other simple experimental tests (Romani et al. 2015). Experimental data provided in Romani et al. (2015) have been used to provide reference solutions associated with onset of cracks in plaster structures containing drilled holes in compression or

in three-point bending of a beam. We also discuss the influence of other numerical parameters on the solution provided by the phase field method such as the size of load increments and the mesh size. Note that complementary results related to this work can be found in a recent paper by Mary et al. (2015).

In the following, we first give a brief summary of the phase field method in Sect. 2. In Sect. 3, we discuss the influence of the main parameters in the numerical method on the predicted mechanical response of cracked structures and show more specifically the relationship between the regularization parameter in the phase field method and some material parameters. In Sects. 4, 5 and 6, we provide qualitative and quantitative comparisons between experimental data of crack initiation in plaster samples with simulations.

2 Mechanical model and numerical simulation method

In the following, the basic concepts of the phase field method are briefly summarized. For more details and practical implementation aspects, the interested reader can refer to Miehe et al. (2010) and Nguyen et al. (2015). The phase field method is based on a regularized formulation of a sharp crack description. A regularized variational principle describing both the evolution of the mechanical problem and of an additional field d describing the damage (called phase field), is discretized by a finite element procedure and a staggered algorithm , chosen here due to its easier implementation. The method alleviates the shortcomings of remeshing crack geometry by using a fixed mesh and a regularized description of the discontinuities. In addition, crack initiation can be modeled in a straightforward manner. In contrast to volume damage models, usually implemented in nonlinear codes, such regularized approach is directly connected to the brittle crack theory of crack propagation. In the present work, the phase field method has been implemented in a in-house code both in 2D and 3D.

In the phase field method, assuming small strains, the regularized form of the energy describing the cracked structure is expressed by:

$$E(\mathbf{u}, d) = \int_{\Omega} W(\mathbf{u}, d) \mathrm{d}\Omega + g_c \int_{\Omega} \gamma(d) \mathrm{d}\Omega, \qquad (1)$$

where W is the density of the elastic energy, depending on the displacements $\mathbf{u}(\mathbf{x})$ and on the phase field $d(\mathbf{x})$ describing the damage of the solid, g_c is the fracture resistance and $\gamma(d)$ is the crack energy density, defined by $\gamma(d, \nabla d) = \frac{1}{2l}d^2 + \frac{l}{2}\nabla d \cdot \nabla d$ (see e.g. Miehe et al. 2010; Nguyen et al. 2015).

Applying the principle of maximum dissipation and energy minimization (Francfort and Marigo 1998) to (1) yields the set of coupled equations to be solved on the domain Ω associated with the structure, with boundary $\delta\Omega$ and outward normal $\mathbf{n}$, to determine $d(\mathbf{x})$ and $\mathbf{u}(\mathbf{x})$, $\forall \mathbf{x} \in \Omega$:

$$
\begin{cases}
2(1-d)\mathcal{H} - \frac{g_c}{l}\left\{d - l^2 \Delta d\right\} = 0 & \text{in } \Omega, \\
d(\mathbf{x}) = 1 & \text{on } \Gamma, \\
\nabla d(\mathbf{x}) \cdot \mathbf{n} = 0 & \text{on } \partial\Omega,
\end{cases}
\tag{2}
$$

and

$$
\begin{cases}
\nabla \cdot \boldsymbol{\sigma}(\mathbf{u}, d) = \mathbf{f} & \text{in } \Omega, \\
\mathbf{u}(\mathbf{x}) = \overline{\mathbf{u}} & \text{on } \partial\Omega_u, \\
\boldsymbol{\sigma}\mathbf{n} = \overline{\mathbf{F}} & \text{on } \partial\Omega_F.
\end{cases}
\tag{3}
$$

In (2), Γ refers to the crack surface, l is the regularization parameter. The history strain energy density function $\mathcal{H}(t)$ is introduced to describe a dependence on history (Miehe et al. 2010) and possible loading-unloading. This function reads:

$$
\mathcal{H}(\mathbf{x}, t) = \max_{\tau \in [0,t]}\left\{\Psi^+(\mathbf{x}, \tau)\right\},
\tag{4}
$$

In (4), Ψ^+ is the tensile part of the elastic strain density function serving to model unilateral contact. It is defined as

$$
\Psi^+(\boldsymbol{\varepsilon}) = \frac{\lambda}{2}\left(\langle Tr(\boldsymbol{\varepsilon})\rangle_+\right)^2 + \mu Tr\left\{\left(\boldsymbol{\varepsilon}^+\right)^2\right\},
\tag{5}
$$

where $\boldsymbol{\varepsilon}$ is the linearized strain tensor and $\langle x \rangle_\pm = (x \pm |x|)/2$ and $\boldsymbol{\varepsilon}^\pm$ are compression and tensile parts of the strain tensor (see e.g. Miehe et al. 2010; Nguyen et al. 2015). The choice of the numerical parameter l is a central issue in the method, which is precisely discussed in the present work.

In (3), $\boldsymbol{\sigma} = \frac{\partial W}{\partial \boldsymbol{\varepsilon}}$ is the second-order Cauchy stress tensor, $\mathbf{f}$ are body forces and $\overline{\mathbf{u}}$ and $\overline{\mathbf{F}}$ are prescribed displacements and forces on the corresponding boundaries $\partial\Omega_u$ and $\partial\Omega_F$, respectively. The symbols $\nabla(.)$ and $\nabla \cdot (.)$ denote gradient and divergence operators, respectively. The constitutive law is expressed (see e.g. Nguyen et al. 2015) by:

$$
\boldsymbol{\sigma} = \left((1-d)^2 + k\right)\left\{\lambda \langle Tr\boldsymbol{\varepsilon}\rangle_+ \mathbf{1} + 2\mu\boldsymbol{\varepsilon}^+\right\}
$$
$$
+ \lambda \langle Tr\boldsymbol{\varepsilon}\rangle_- \mathbf{1} + 2\mu\boldsymbol{\varepsilon}^-
\tag{6}
$$

where k is a small numerical parameter to avoid loss of stability in case of fully damaged elements.

Equations (2)–(3) are solved by a standard FE procedure in a staggered scheme at each time step (load increment). More theoretical and practical details can be found e.g. in Miehe et al. (2010) and Nguyen et al. (2015).

3 Discussion on the influence of input parameters in the numerical simulations

In this section, we discuss the influence of the numerical parameters on the simulation results. More specifically, we study the influence of: (a) the mesh size, (b) the loading increments size, (c) the regularization parameter l in (2). For this purpose, we consider a benchmark problem with features similar to that of the experimental tests studied in the following. The benchmark described in Fig. 1 consists into a drilled sample subjected to compression. Compression tests are often preferred to tensile ones in civil engineering because of their better stability during crack propagation (see e.g. Sammis and Ashby 1986; Wong et al. 2006). More details about the real corresponding experimental test are provided in the following. The geometry of the sample and boundary conditions are depicted in Fig. 1. The material parameters have been chosen as $E = 12\,\text{GPa}$, $v = 0.3$ and $g_c = 1.4\,\text{N/m}$ from the experimental values provided in Romani et al. (2015). Plane strain conditions are assumed.

3.1 Influence of the mesh size

In a first test, we investigate the convergence of the mechanical response with respect to mesh refinement. In all examples of this work, linear elements have been used, i.e. triangles in 2D and tetrahedra in 3D. Here, the regularization parameter is fixed to $l = 0.1$ mm. We discuss in the following how to choose this parameter. It has been shown in Miehe et al. (2010) that given l, the criterion
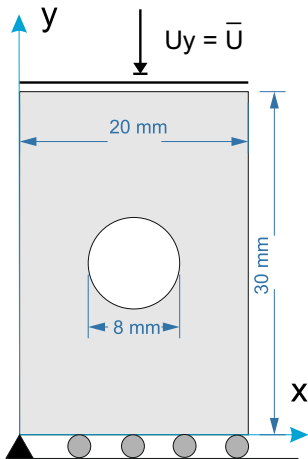
$$
h \leq l/2
\tag{7}
$$

Fig. 1 Benchmark problem for analyzing the influence of numerical parameters on the simulation results: geometry and boundary conditions
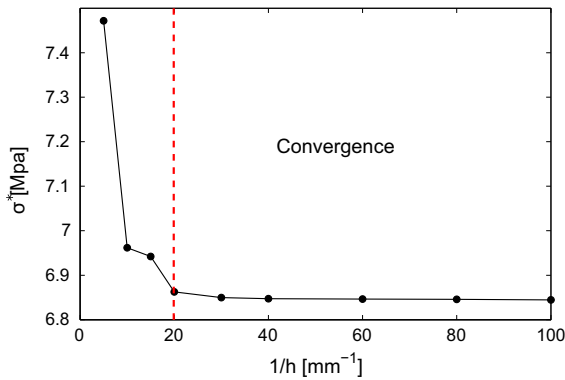

Fig. 2 Convergence of the solution with respect to mesh size

must be fulfilled. Monotonic compressive displacement increments of $\Delta \overline{U} = -1 \times 10^{-4}$ mm have been prescribed for 250 load increments. Then we have performed several simulations using refined meshes, where the characteristic size of the elements vary between $h = 0.01$ mm and $h = 0.1$ mm. Let us define the overall critical axial stress σ^* as the ratio of the y-component of the resultant force prescribed at the top of the sample to the area of its upper face, when damage reaches the value $d = 1$ for the first load increment at some node in the mesh (i.e. stress associated to the onset of the first crack). We study in Fig. 2 the convergence of this quantity with respect to mesh size. A clear convergence is observed, with results becoming mesh independent when condition (7) is fulfilled. This confirms the results of Miehe et al. (2010).

3.2 Influence of the load increments

Next, we analyze the influence of the load increment $\Delta \overline{U}$ in the numerical simulation on the mechanical response. We have used several load increments from $\Delta \overline{U} = 1.5 \times 10^{-3}$ mm to $\Delta \overline{U} = 3 \times 10^{-5}$ mm. Results are presented in Fig. 3. In Fig. 3b, we study the evolution of σ^* with respect to $\Delta \overline{U}$ and can note the related convergence: the variation of σ^* is below 2 % when the increment goes from 5.10^{-5} to 3.10^{-5} mm. This confirms the stability of the easy-to-implement staggered algorithm as soon as sufficiently small loading steps are used. Too large steps tend to delay the initiation of damage and thus harden the overall response of the structure.

3.3 Choice of the regularization parameter l

In the following, we show that the regularization parameter l in (2) depends on material parameters. To illustrate this point, we consider a bar under uniaxial traction as depicted in Fig. 4. We assume that the Poisson ration is zero. In this configuration and in the absence of initial defects, the damage distribution is assumed to be homogeneous, i.e. $\nabla d(\mathbf{x}) = 0$.

Assuming an isothermal process, the reduced form of the Clausius-Duhem inequality can be written as:

$$\mathcal{A}\dot{d} \geq 0 \tag{8}$$

where

$$\mathcal{A} = -\frac{\partial E}{\partial d} \tag{9}$$

is the thermodynamic force associated with d and $\dot{d}$ denotes derivative with respect to time t. We assume that the evolution of the damage parameter d is governed by the simple negative threshold function

$$F(\mathcal{A}) = \mathcal{A} \leq 0, \tag{10}$$

such that when $F(\mathcal{A}) < 0$ no evolution of damage occurs. The principle of maximum dissipation requires the dissipation $\mathcal{A}\dot{d}$ to be maximum under the constraint (10). By using the method of Lagrange multipliers, we define the Lagrangian as:

Fig. 3 Convergence of the solution with respect to the displacement increments in the numerical simulation: **a** load-displacement curve; **b** σ^* for various displacement increments

(a)

(b)
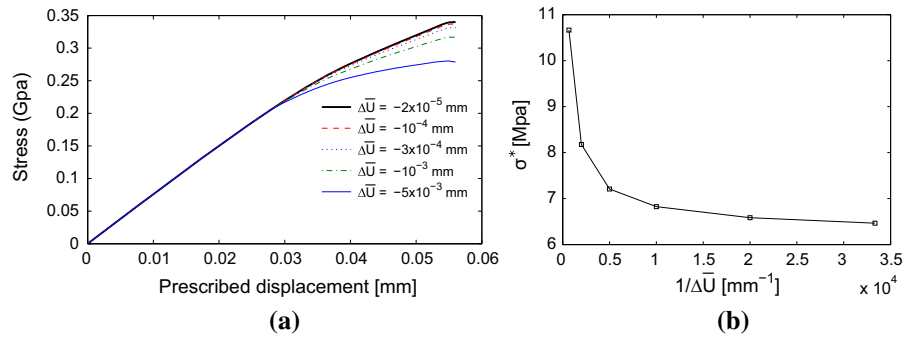
$$\mathcal{L} = -\mathcal{A}\dot{d} + \lambda F(\mathcal{A}) \qquad (11)$$

where λ is the Lagrange multiplier associated with the constraint (10). Minimizing $\mathcal{L}$ under the constraint (10) yields the Kuhn-Tucker equalities:

$$\frac{\partial \mathcal{L}}{\partial \mathcal{A}} = 0, \quad \lambda \geq 0, \quad F \leq 0, \quad \lambda F = 0. \qquad (12)$$

The left-hand equation in (12) gives $\lambda = \dot{d}$. Then for $\dot{d} > 0$, $F(\mathcal{A}) = 0 = \mathcal{A} = -\frac{\partial E}{\partial d}$, which leads to (see more details in Nguyen et al. 2015):

$$F = 2(1-d)\Psi^+ - g_c\delta\gamma(d) = 0. \qquad (13)$$

In (13), $\delta\gamma(d)$ is given by $\delta\gamma = \frac{d}{l} - l\Delta d$ (Miehe et al. 2010), where Δd is the Laplacian of d. For a uniform damage parameter as in the considered 1D problem, $\delta\gamma$ reduces to $\delta\gamma = d/l$.

For uniaxial tension, and assuming $k \simeq 0$ we can write from (6):

$$\sigma = g(d)E\varepsilon, \quad \Psi^+ = \frac{1}{2}E\varepsilon^2, \qquad (14)$$

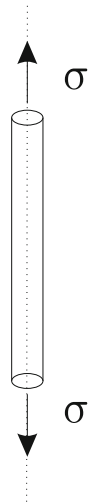with $g(d) = (1-d)^2$. Then using (13), we obtain the relation:

$$(1-d)E\varepsilon^2 - \frac{g_c}{l}d = 0. \qquad (15)$$

The strain and stress can then be expressed by:

$$\varepsilon(d,l) = \sqrt{\frac{g_cd}{lE(1-d)}}, \qquad (16)$$

$$\sigma(d,l) = \sqrt{d(1-d)^3}\sqrt{\frac{Eg_c}{l}}. \qquad (17)$$

Fig. 4 1D problem for the analysis of the phase method in an initially homogeneous situation

The maximum value of the stress with respect to d is given by:

$$\sigma_c = \text{Arg}\left\{\sup_{d=[0\ 1]} \sigma(d,l)\right\} \qquad (18)$$

which is reached for $d = 1/4$, corresponding to the critical value of the stress σ_c:

$$\sigma_c = \frac{9}{16}\sqrt{\frac{Eg_c}{3l}} \qquad (19)$$

and of the strain:

$$\varepsilon_c = \sqrt{\frac{g_c}{3lE}} \qquad (20)$$

These obtained formulations are similar with the result in the work of Amor et al. (2009). Analyses leading to similar relationships can also be found in Kuhn et al. (2015), Benalla and Marigo (2007), Borden

Fig. 5 Evolution of the solution with respect to the regularization parameter l: **a** Load-displacement curve; **b** σ^* versus l
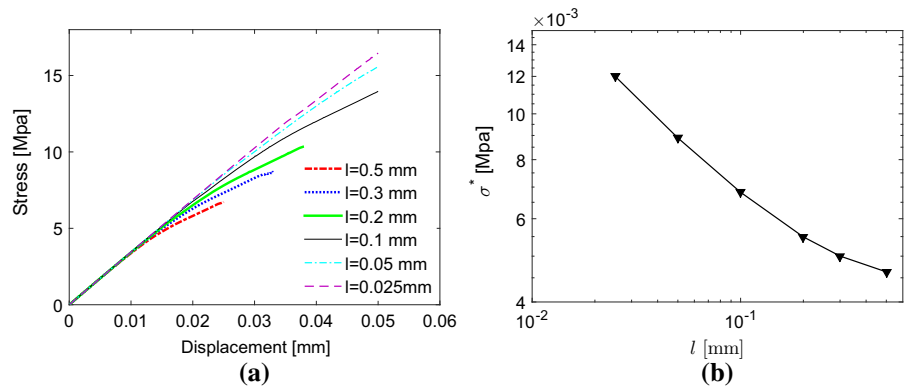
et al. (2012) and Pham et al. (2011). From these expressions, it is clear that the critical stress will increase as l decreases. In the limit of l tending to zero, i.e., when the phase-field formulation coincides with the discrete fracture formulation, the crack nucleation stress becomes infinite. This observation is consistent with the predictions of Griffith's theory, which only allows for crack nucleation at stress singularities. Equation (20) gives a relationship between l and the material parameters, namely the Young modulus, E, the Griffith critical surface energy, g_c, and a value of the tensile strength σ_c determined experimentally, and denoted in that case by σ_c^{exp}, which now refers to the critical stress leading to rupture in a uniaxial uniform tension test:

$$l = \frac{27 E g_c}{256 \left(\sigma_c^{exp}\right)^2}. \qquad (21)$$

Note that this relation holds for uniaxial traction without damage gradient and only provides an estimation for l but clearly shows that l can be linked to material parameters. From the values of g_c and σ_c^{exp} identified experimentally in Romani et al. (2015) for a plaster material, i.e. $E = 12\,\text{GPa}$, $\sigma_c = 3.9\,\text{MPa}$ and $g_c = 1.4\,\text{N/m}$ we obtain $l \simeq 0.1\,\text{mm}$.

In the next test, we show numerically that the mechanical response does not converge with respect to the parameter l. An unstructured mesh with minimal element size $h_{min} = 0.01\,\text{mm}$ is employed around the hole where the cracks should initiate, and with maximal element size $h_{max} = 1\,\text{mm}$ away from the hole, such that mesh size ensures numerical convergence of the computations for all values of l considered hereafter. The displacement increment is chosen as $\Delta \overline{U} = 10^{-4}\,\text{mm}$. In Fig. 5a, the evolution of the
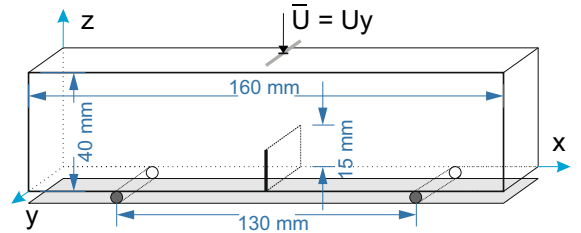

Fig. 6 3D 3-point bending test: geometry and boundary conditions

solution with respect to the regularization parameter l is plotted for different values of l ranging from 0.025 to 0.5 mm. In Fig. 5b, the stress required to onset the first crack σ^* is plotted versus l. While the force-displacement curve in Fig. 5a seems to converge when l decreases (indeed towards a purely elastic response), it is obvious that this is not the case for the value of σ^*. This test illustrates the fact that the regularization parameter l must be identified as a material parameter, i.e. each value of l will lead to a different response of the structure.

4 Experimental validation: three-point bending test

4.1 Pre-notched beam

In this test, we validate the phase field solution on an experimental 3-point bending test of a beam containing an initial crack of length 15 mm. The geometry, dimensions, and boundary conditions of the structure are depicted in Fig. 6. The material is dry plaster, composed of plaster powder of the Siniat Company named Prestia Profilia 35®. The plaster sample prepa-
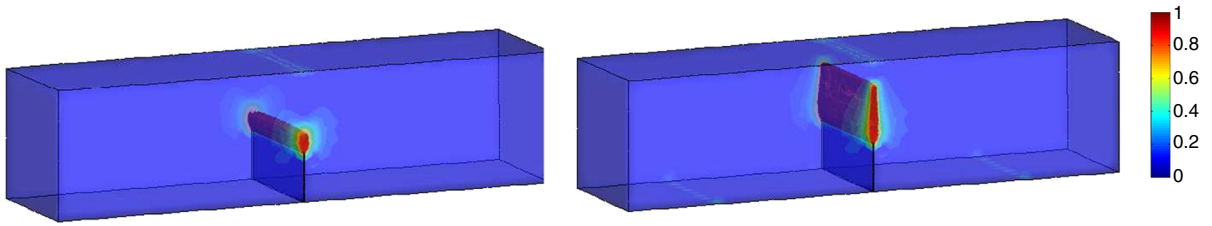
Fig. 7 3-point bending test, crack evolution (damage variable $d(\mathbf{x})$) for two prescribed displacements: $\overline{U} = 0.15\,\mathrm{mm}$ and $\overline{U} = 0.18\,\mathrm{mm}$

ration are detailed in a previous work (Romani et al. 2015). In the mentioned study, the material parameters have been identified experimentally and are the same as in the previous example: $E = 12\,\mathrm{GPa}$, $\nu = 0.3$, $g_c = 1.4\,\mathrm{N/m}$ and $\sigma_c^{exp} = 3.9\,\mathrm{MPa}$, which give the value of $l = 0.1\,\mathrm{mm}$ from (21). Note that here the Poission ratio is non zero and the problem is not one-dimensional, thus (21) only provides an estimation for l. In addition, it is worth noting that the derivation of (21) is only valid for a benchmark case involving homogeneous displacements and $d(\mathbf{x})$ field before fracture nucleation.

The z−component of displacements $\overline{U}$ is prescribed along a line in the middle of the upper face, while the all components of displacements are blocked along two lines on the lower face (see Fig. 6).

Three-dimensional simulations have been conducted. A refined mesh was constructed using tetrahedral elements, with $h_{\max} = 3\,\mathrm{mm}$ and $h_{\min} = 0.05\,\mathrm{mm}$ in the region of expected crack path, to satisfy the condition $h_{\min} \leq l/2$. Monotonic compressive displacement increments of $\Delta\overline{U} = -5 \times 10^{-4}\,\mathrm{mm}$ have been prescribed as long as $d < 0.9$ in all elements and $\Delta\overline{U} = -5 \times 10^{-5}\,\mathrm{mm}$ as soon as $d > 0.9$ in one integration point. The crack propagation evolution is depicted in Fig. 7 for two loading stages.

Figure 8 provides the load-displacement curve obtained from the simulation. The critical load F_r is defined as the maximum resultant load before softening due to crack propagation. We compare this critical load with the experimental values provided in Romani et al. (2015) for several samples in Fig. 9 and can note that we obtain a good agreement for the values of F_r with respect to experiments.
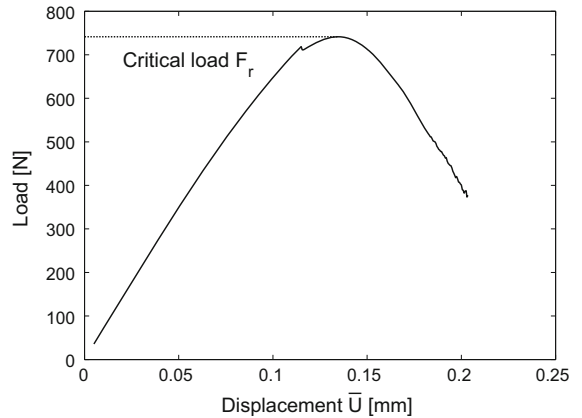

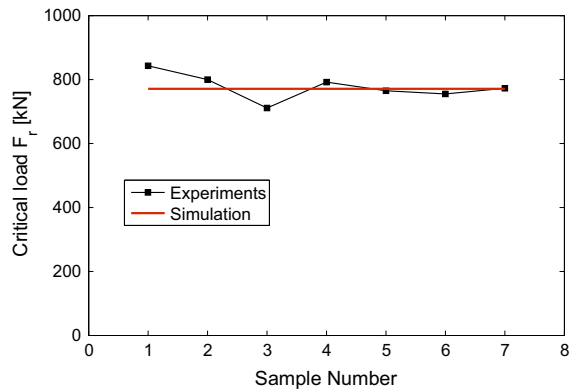**Fig. 8** Load-displacement curve for the 3-point bending test: numerical model

Fig. 9 Critical load for the 3-point bending problem: comparison between experiments and numerical predictions

4.2 Un-notched beam

We investigate now the capability of the phase field method to provide a correct estimated value of σ_c^{exp}
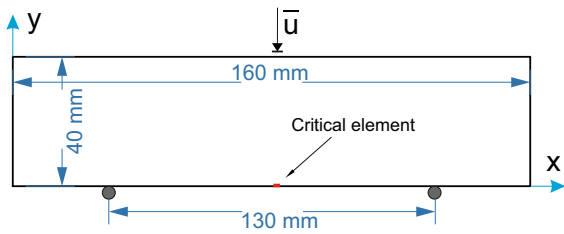
Fig. 10 2D 3-point bending test of non cracked beam: Geometry and boundary conditions
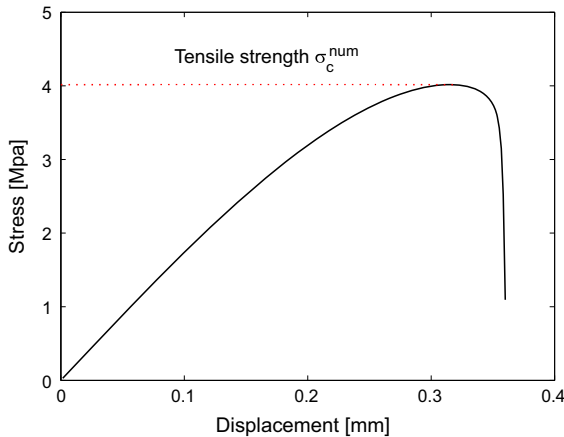

Fig. 11 Tensile strength for the 3-point bending problem: stress–displacement curve of the critical element

Fig. 12 Plaster sample containing one cylindrical drilled hole: geometry and boundary conditions for both experimental setup and simulation

5 Experimental validation: compression of a drilled plaster specimen containing a single cylindrical hole

In the following, we investigate crack initiation and propagation in a more involved test, and compare the numerical prediction with experimental results provided in Romani et al. (2015). The objective is to evaluate if the numerical model is able to predict accurately the response of cracked structure in other configurations than the ones used to identify the material parameters.

A drilled sample is considered, as depicted in Fig. 12. A thick plate contains one single cylindrical hole with diameter D. Several samples with various hole diameters, ranging from $D = 3$ to $D = 6$ mm, have been tested. The dimensions of the plate are 100 mm × 65 mm × 40 mm. The material (plaster) is the same as in the previous example. The sample is loaded in compression. In the experimental tests, the load is applied continuously at a speed of 0.2 mm/min. Consistently, the numerical calculations are run in the quasi static regime, as for previous cases. PMMA plates were used on top and bottom face to reduce the lack of planarity, parallelism and friction conditions (Romani 2013) to avoid stress concentration.

Experimental image correlation data were provided in Romani et al. (2015), together with force measurement to detect the crack experimentally. A high-resolution camera (Baumer HXC20, progressive scan sensor with 2048 × 1088 pixels), with a pixel size of

for crack initiation in a structure different from the one in which the critical stress σ_c^{num} was identified. For this purpose, we consider an un-cracked beam under three-point bending, as depicted in Fig. 10.

The stress is evaluated numerically during the simulation in an element located on the known path of the crack. The tensile strength σ_c^{num} is defined as the maximal stress evaluated numerically before softening in the integration point of an element located in the middle of the lower end, as depicted in Fig. 11. In the present work, we have used linear finite elements, with one Gauss integration point per element. From now on and in all following examples, all material parameters are the same as in the previous example and l is equal to 0.1 mm. Monotonic compressive displacement increments of $\Delta \overline{U} = -2 \times 10^{-3}$ mm have been used for 180 increments. We obtain a good agreement between the value predicted numerically ($\sigma_c^{num} = 4.01$ MPa) and the experimental value identified from another experiment in Romani et al. (2015) ($\sigma_c^{exp} = 3.9$ MPa).
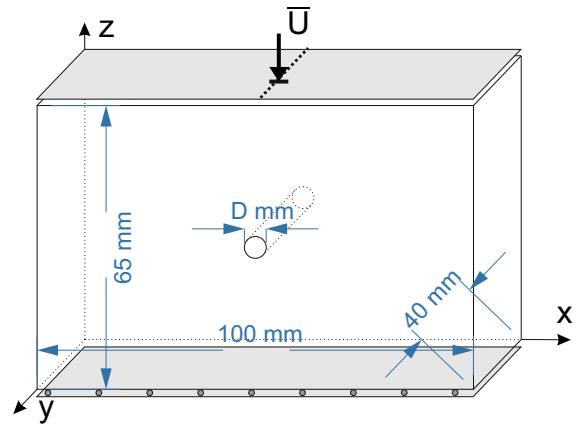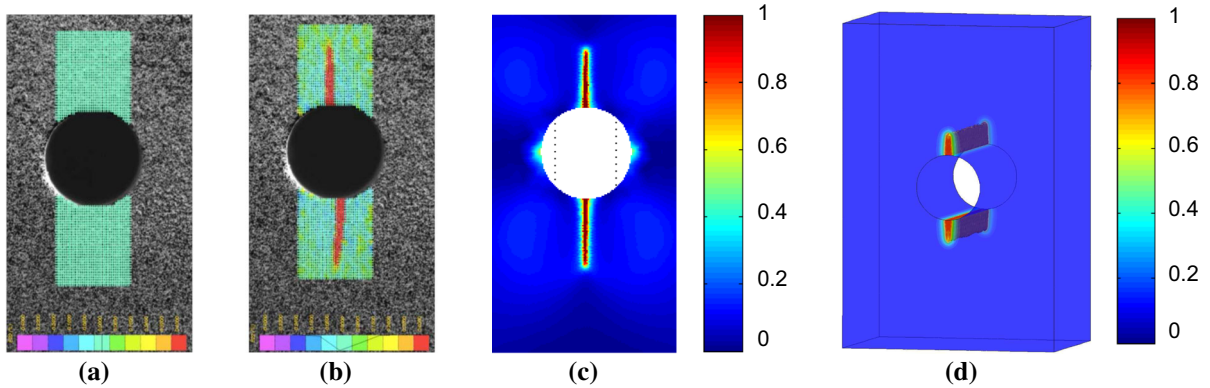
Fig. 13 Crack path evolution near the cylindrical hole ($D = 5$ mm); **a**, **b** strain maps obtained with digital image correlation for initial and loaded state (Romani et al. 2015), for 15.2 and 14.1 MPa, respectively; **c** 2D simulation (plane strain); **d** 3D simulation (damage variable $d(\mathbf{x})$)

5.5×5.5 μm^2, and equipped with a ZEISS Makro-Planar 100 mm macro lens was used to continuously acquire images of the specimen during loading at a frame rate of 20 Hz. As the detection of the crack onset is not possible with naked eye, the recorded images were processed by 2D digital image correlation (DIC) techniques. Cracks are detected by high levels of local xx−strain components, measured for a gage length defined by the mesh of correlation points (20 pixels spacing), which is the signature of the presence of displacement discontinuities between two points of the mesh.

The 2D technique of digital image correlation 2D-DIC was used. When the sample is subjected to a compressive load, two opposite cracks initiate on top and bottom of the hole and grow from the cavity, in a direction parallel to the load. In Romani et al. (2015), the experimental results have been compared to the semi-analytical model of Leguillon (2002), which requires numerical FEM computations to evaluate the stress intensity factors. In the mentioned work, 2D FE simulations with plane strain assumptions were used. In view of the dimensions of the sample and owing to the fact the measurements are performed at the surface of the sample, the plane strain assumption might be questionable. For this purpose, we have performed 2D simulations with both plane strain and plane stress assumption, as well as full 3D simulations. The boundary conditions model the experimental ones on the sample, and are described for the 3D case in Fig. 12: on the lower surface ($z = 0$), the z-displacements are

fixed and the x- and y-displacements are free. On the upper end, the x- and y-displacements are free, while the z-displacements are prescribed, with an increasing value $\overline{U}$ during the simulation. Monotonic compressive displacement increments of $\Delta\overline{U} = -10^{-3}$ mm are prescribed for first load increments and as soon as d reaches 0.9 in one integration point of the Finite Element mesh, we use $\Delta\overline{U} = -10^{-4}$. A finite element mesh with varying element size ($h_{min} = 0.05$ mm around the hole and $h_{max} = 0.25$ mm in the rest of domain) is used.

In Figs. 13 and 14, we show a comparison of the experimental digital image correlation technique used to detect the crack evolution and the simulation, were the damage field, associated with the crack, is depicted. This case corresponds to a diameter $D = 5$ mm. We can note that the numerical solution based on the phase field method can capture the crack initiation on top and bottom of the hole and the vertical path of the two cracks. In addition, the length of the crack for the given load is accurately predicted (Fig. 13b, c).

In the simulations, the crack length is computed as the distance between the last point for which $d = 1$ and the hole boundary, assuming a straight crack. The same procedure is employed in 3D. In Fig. 15 we quantitatively compare the crack length evolution with respect to the applied load computed at the point where the displacement is prescribed. Results for 2D plane strain and plane stress, 3D simulations and experimental DIC results are compared in Fig. 14. Figure 15 shows that all three models provide a satisfying prediction for the

Fig. 14 Crack propagation at different values of the applied stress around the cylindrical hole: comparison between experiments (digital image correlation) and simulations (damage variable $d(\mathbf{x})$)
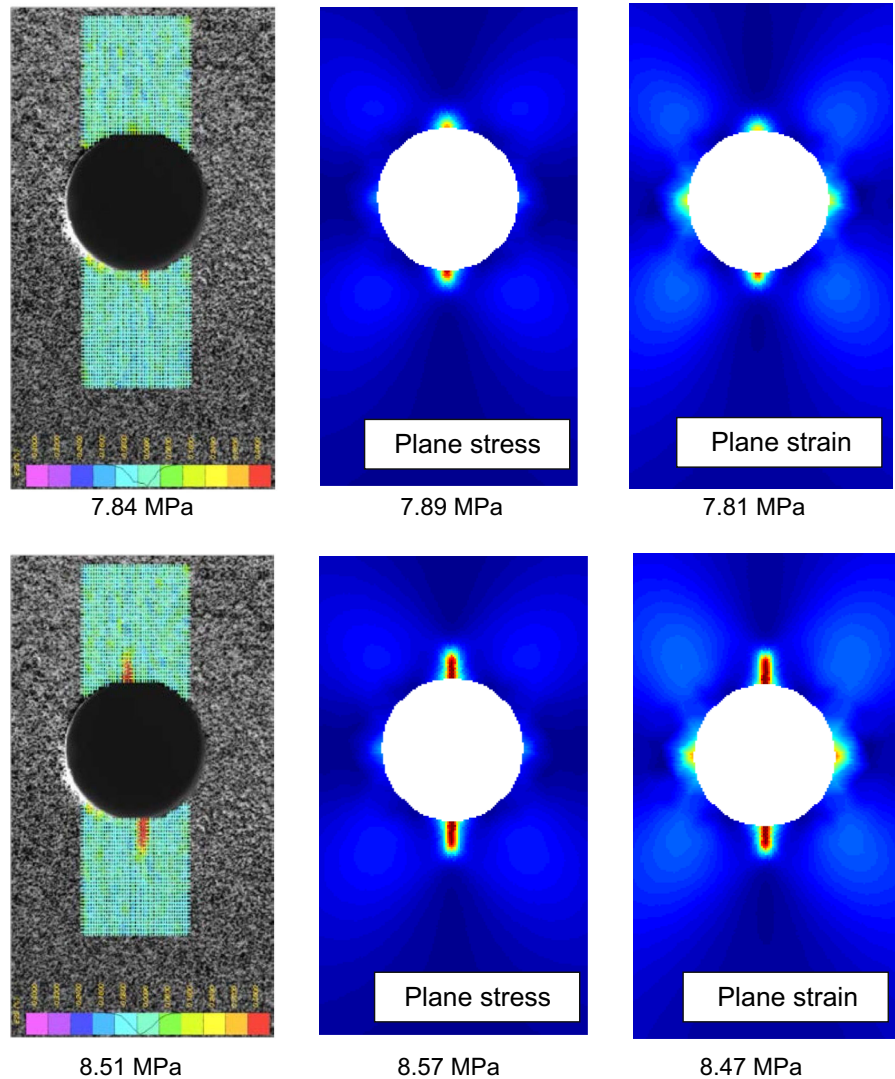
critical load corresponding to the onset of the crack. However, we can note that during propagation, the experimental evolution deviates from 2D predictions. The 3D simulation is in that case in better agreement with the experimental response for both top and bottom cracks.

To analyze the influence of the diameter of the hole on the stress at the time cracks onset, several samples with diameters varying between 3 and 6 mm have been prepared and tested. Simulations have been performed here also in 2D and 3D. Results are provided in Fig. 16. They show the good ability of the simulation model to accurately predict the evolution of critical load σ^* (onset of the crack) with hole diameters and related size effects. Size effects in the context of the phase

field method have been investigated in Kuhn and Müller (2014). The quality of different strength criteria has been examined with respect to experimental data for samples with several hole diameters in Li and Zhang (2006). In the mentioned work, the authors discussed the validity of one, two and three parameters criteria to model size effects.

6 Microcracking in a plaster specimen containing a periodic distribution of cylindrical holes

In this last example, we investigate the microcracking of two plaster specimens containing many holes, whose configurations are depicted in Fig. 17. In both

Fig. 15 Evolution of the crack length with respect to the resultant stress on the upper boundary, comparison between models and experimental data: **a** top crack; **b** bottom crack
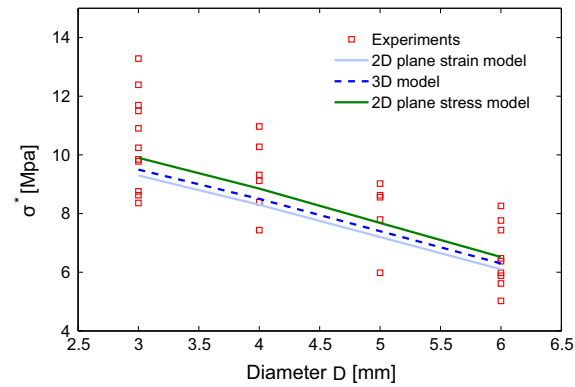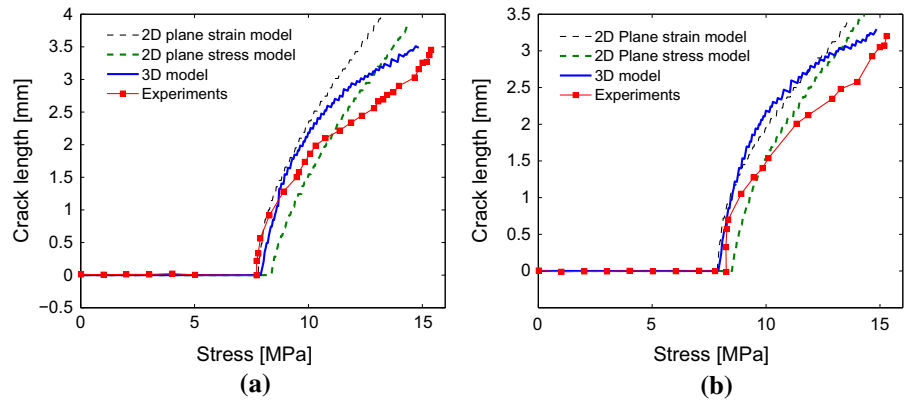

(a)

(b)

Fig. 16 Stress associated with the cracks onset with respect to the cylindrical hole diameter: comparison between experiments and numerical simulation

cases, the diameter of the holes is $D = 4$ mm. Configuration of Fig. 17a corresponds to a volume fraction of 12.2%, and in Fig. 17b to 13.5%. A FE adaptive mesh with characteristic size $h_{min} = 0.05$ mm has been used around the holes, and larger elements whose size are $h_{max} = 0.5$ mm have been employed away from holes. The whole mesh contains 905437 elements.

2D plane strain simulation was conducted. Monotonic compressive displacement increments are prescribed on the top edge of the specimen, with $\Delta \overline{U} = -10^{-3}$ mm in the first 1000 increments and $\Delta \overline{U} = -5 \times 10^{-5}$ mm in the last 1500 increments. The evolution of microcracking within the specimen is depicted in Fig. 18. The simulation model captures well the vertical propagation of the different microcracks. The microcracks propagate faster near the left and right boundaries than in the central region, probably because

of the influence of the free boundary conditions on the lateral surfaces. In addition, there is also a slight dissymmetry between upper and lower parts of the sample (a), whose successive damage maps are reproduced in Fig. 18. This is linked to the absence of horizontal symmetry for this sample. For sample (b), the hole distribution is symmetric between upper and lower parts, and the resulting simulated damage map is also symmetric.

In Fig. 19 the microcracking pattern for the case of porous fraction 13.5% is depicted and numerical simulations and digital correlation image obtained in Romani (2013) are qualitatively compared. Globally speaking, the heterogeneity of the damage map between central and lateral parts of the sample is nicely captured by the computation. In Fig. 20, we compare with more details the microcracking morphology between the simulation and the experiment provided in Romani (2013) and Romani et al. (2015), and note that it is qualitatively captured, both regarding the vertical propagation of the different cracks, and regarding the non uniform propagation of the microcracks within the sample.

To compare more quantitatively the predictions provided by the numerical simulation, we analyze the effects of changing the configuration (volume fraction and distribution) with respect to the stress required to initiate the first cracks in the sample and to generate cracks around all holes. Again, the corresponding experimental values have been provided in Romani (2013). Comparisons are provided in Fig. 21. The numerical simulation method is in good agreement with the experimental values.
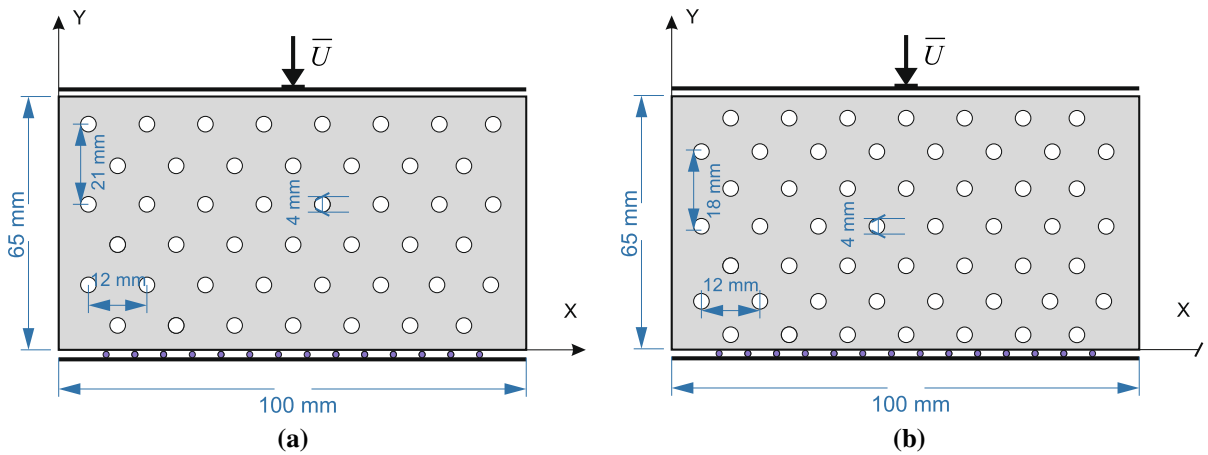
Fig. 17 Plaster specimen containing a regular distribution of cylindrical holes: **a** surface fraction 12.2 % and **b** surface fraction 13.5 % (Romani 2013)

Fig. 18 Plaster specimen containing regular distribution of cylindrical holes: evolution of the microcracking for different compressive loads (damage variable $d(\mathbf{x})$): **a** $\overline{U} = 0.544$ mm; **b** $\overline{U} = 0.594$ mm; **c** $\overline{U} = 0.64$ mm; **d** $\overline{U} = 0.67$ mm;
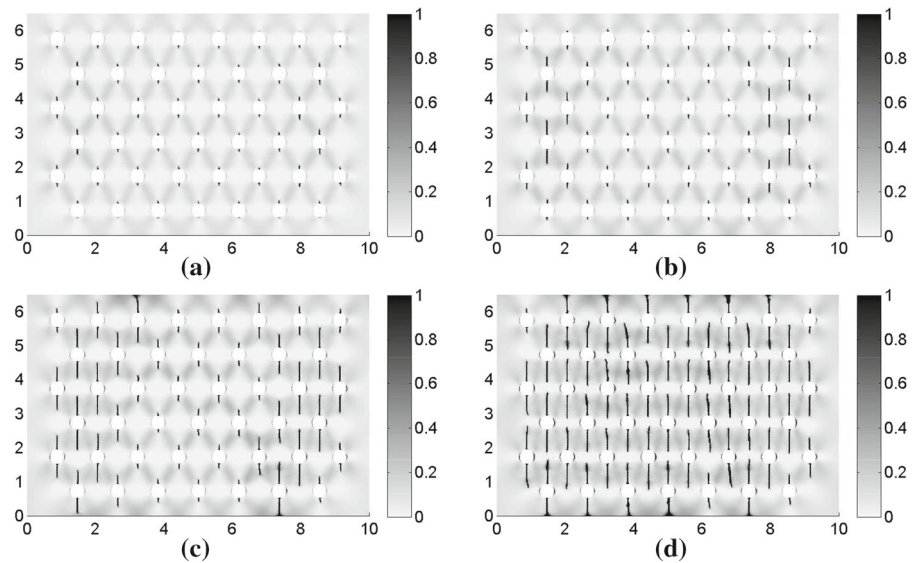

Fig. 19 Crack trajectory comparison between the present simulation (**a**) and the experiment (**b**) provided in Romani (2013) (damage variable $d(\mathbf{x})$) for $\overline{U} = 0.614$ mm
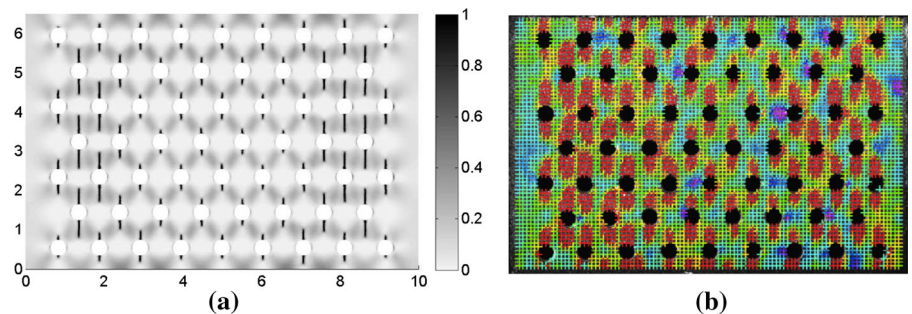
Fig. 20 Qualitative comparison of the microcracking propagation between the present simulation and the experiment provided in Romani (2013) (damage variable $d(\mathbf{x})$) for $\overline{U} = 0.64$ mm
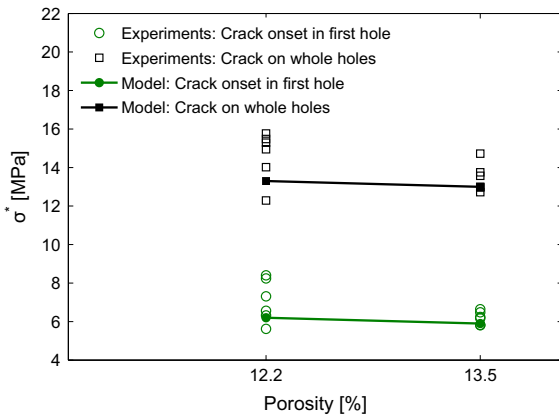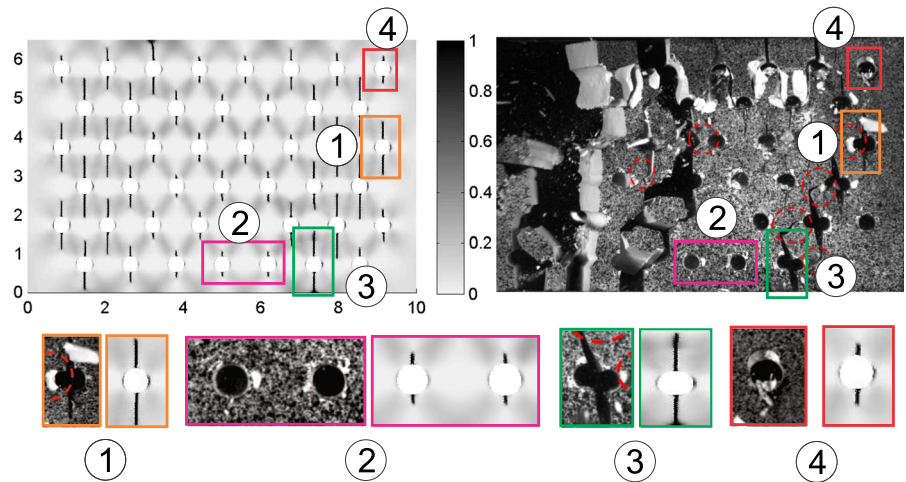

Fig. 21 Stress corresponding to crack onset within the specimen: comparison between experimental results and the numerical model for two porosities

7 Conclusion

In this work, we have discussed the choice of the parameters in the phase field method, which is a promising simulation tool for initiation and propagation of cracks in brittle materials. More specifically, we have analyzed the influence of the numerical parameters and have validated the fact that the regularization parameter describing the width of the smeared crack approximation is linked to material parameters. The regularization length then requires experimental measures to be identified. We have shown that the other numerical parameters (load increments, mesh size) lead to convergent responses when they decrease. Then, from the knowledge of the elastic parameters, of the fracture resistance

and of the regularization parameter of the phase field method, essentially identified from experimental measurements of critical stress in uniformly stressed samples, we have conducted several simulations, including crack initiation and propagation in three-point bending beam and in drilled samples of plaster in compression. Remarkably, the phase field model is able to predict quantitatively crack paths, crack propagation morphologies, and mechanical response with good agreement regarding experimental results for other geometrical configurations than the ones used to identify the material parameters. Thus, the phase field method constitutes a promising tool for prediction of strength in brittle heterogeneous or lightweight materials for civil engineering.

References

Amor H, Marigo JJ, Maurini C (2009) Regularized formulation of the variational brittle fracture with unilateral contact: numerical experiments. J Mech Phys Solids 57(8):1209–1229

Bažant Z, Belytschko T (1985) Wave propagation in strain-softening bar: exact solution. J Eng Mech 111:81–389

Bažant Z, Pijaudier-Cabot G (1988) Nonlocal continuum damage, localization instability and convergence. J Appl Mech 55:521–539

Belytschko T, Black T (1999) Elastic crack growth in finite elements with minimal remeshing. Int J Numer Methods Eng 45:601–620

Benalla A, Marigo J-J (2007) Bifurcation and stability issues in gradient theories with softening. Model Simul Mater Sci 15(1):S283–S295

Bernard PE, Moës N, Chevaugeon N (2012) Damage growth modeling using the thick level set (TLS) approach: efficient discretization for quasi-static loadings. Comput Methods Appl Mech Eng 233:11–27

Borden MJ, Verhoosel CV, Scott MA, Hughes TJR, Landis CM (2012) A phase-field description of dynamic brittle fracture. Comput Methods Appl Mech Eng 217:77–95

Bourdin B (2007) Numerical implementation of the variational formulation for quasi-static brittle fracture. Interface Free Bound 9(3):411–430

Camacho G, Ortiz M (1996) Computational modelling of impact damage in brittle materials. Int J Solids Struct 33:2899–2938

Cazes F, Moës N (2015) Comparison of a phase-field model and of a thick level set model for brittle and quasi-brittle fracture. Int J Numer Methods Eng (in press)

Daux C, Moës N, Dolbow J, Belytschko T (2000) Arbitrary branched and intersecting cracks with the extended finite element method. Int J Numer Methods Eng 48:1741–1760

De Borst R, Sluys lJ, Muhlausanf HB, Pamin J (1993) Fundamental issues in finite element analysis of localization of deformation. Eng Comput 10:99–121

Eastgate LO, Sethna JP, Rauscher M, Cretegny T (2002) Fracture in mode i using a conserved phase-field model. Phys Rev E 65(3):036117

Francfort GA, Marigo JJ (1998) Revisiting brittle fracture as an energy minimization problem. J Mech Phys Solids 46(8):1319–1342

Hakim V, Karma A (2009) A continuum phase field model for fracture. J Mech Phys Solids 15(2):342–368

Hofacker M, Miehe C (2013) A phase field model of dynamic fracture: robust field updates for the analysis of complex crack patterns. Int J Numer Methods Eng 93(3):276–301

Kuhn C, Müller R (2010) A continuum phase field model for fracture. Eng Frac Mech 77(18):3625–3634

Kuhn C, Müller R (2014) Simulation of size effects by a phase field model for fracture. Theor Appl Mech Lett 4:051008

Kuhn C, Schlueter A, Müller R (2015) A phase-field description of dynamic brittle fracture. Comput Mater Sci 108:374–384

Lasry D, Belytschko T (1988) Localization limiters in transient problems. Int J Solids Struct 24:581–597

Leguillon D (2002) Strength or toughness? A criterion for crack onset at a notch. Eur J Mech A Solid 21(1):61–72

Li J, Zhang XB (2006) A criterion study for non-singular stress concentrations in brittle or quasi-brittle materials. Eng Frac Mech 73:505–523

Lorentz E, Benallal A (2005) Gradient constitutive relations: numerical aspects and application to gradient damage. Comput Methods Appl Mech Eng 194:5191–5220

Mary S, Vignollet J, de Borst R (2015) A numerical assessment of phase-field models for brittle and cohesive fracture: Γ-convergence and stress oscillations. Eur J Mech A Solids 52:72–84

Miehe C, Hofacker M, Welschinger F (2010) A phasefield model for rate-independent crack propagation: robust algorithmic implementation based on operator splits. Comput Methods Appl Mech 199:2765–2778

Miehe C, Welschinger F, Hofacker M (2010) Thermodynamically consistent phase-field models of fracture: variational principles and multi-field fe implementations. Int J Numer Methods Eng 83(10):1273–1311

Moës N, Dolbow J, Belytschko T (1999) A finite element method for crack growth without remeshing. Int J Numer Methods Eng 46:131–150

Nguyen TT, Yvonnet J, Zhu Q-Z, Bornert M, Chateau C (2015) A phase field method to simulate crack nucleation and propagation in strongly heterogeneous materials from direct imaging of their microstructure. Eng Fract Mech 139:18–39

Nguyen TT, Yvonnet J, Zhu Q-Z, Bornert M, Chateau C (2016) A phase-field method for computational modeling of interfacial damage interacting with crack propagation in realistic microstructures obtained by microtomography. Comput Methods Appl Mech Eng. doi:10.1016/j.cma.2015.10.007

Peerlings RHJ, de Borst R, Brekelmans WAM, de Vree HPJ (1996) Gradient-enhanced damage for quasi-brittle materials. Int J Numer Methods Eng 39(39):3391–3403

Pham K, Marigo J-J, Maurini C (2011) The issues of the uniqueness and the stability of the homogeneous response in uniaxial tests with gradient damage models. J Mech Phys Solids (6)

Pietruszczak S, Mroz S (1981) Finite element analysis of deformation of strain-softening materials. Int J Numer Methods Eng 17:327–334

Pijaudier-Cabot G, Bažant Z (1987) Nonlocal damage theory. J Eng Mech 113:1512–1533

Romani R (2013) *Rupture en compression des structures hétérogènes á base de materiaux quasi-fragiles*. PhD thesis, Université Pierre et Marie Curie

Romani R, Bornert M, Leguillon D, Roy RL, Sab K (2015) Detection of crack onset in double cleavage drilled specimens of plaster under compression by digital image correlation-theoretical predictions based on a coupled criterion. Eur J Mech A Solid 51:172–182

Sammis CG, Ashby WF (1986) The failure of brittle porous solids under compressive stress states. Acta Metall 34(3):511–526

Spatschek R, Hartmann M, Brener E, Müller KH, Kassner K (2006) Phase field modeling of fast crack propagation. Phys Rev Lett 96(1):015502

Triantafyllidis N, Aifantis EC (1986) A gradient approach to localization of deformation: I. Hyperelastic materials. J Elast 16:225–237

Wong RHC, Lin P, Tang CA (2006) Experimental and numerical study on splitting failure of brittle solids containing single pore under uniaxial compression. Mech Mater 38:142–159

Xu X-P, Needleman A (1994) Numerical simulation of fast crack growth in brittle solids. J Mech Phys Solids 42(9):1397–1434

Zhou F, Molinari JF (2004) Dynamic crack propagation with cohesive elements: a methodology to address mesh dependency. Int J Numer Methods Eng 59:1–24